UNIVERSITY OF COPENHAGEN
FACULTY OF SCIENCE
NIELS BOHR INSTITUTE

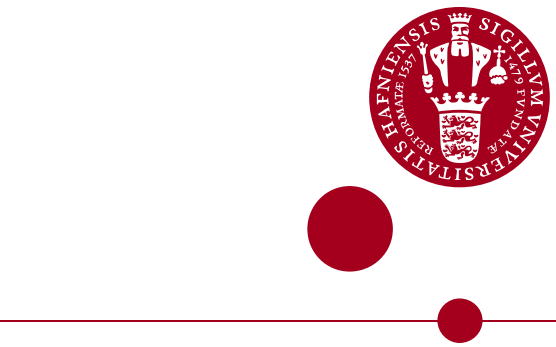

Towards n-Parity Protected Superconducting Qubits using 2D Electron Gas

Billy Lim Jun Ming

Master's Thesis
Center for Quantum Devices
Niels Bohr Institute
University of Copenhagen

Supervisor:
Charles M. Marcus

July 25, 2021

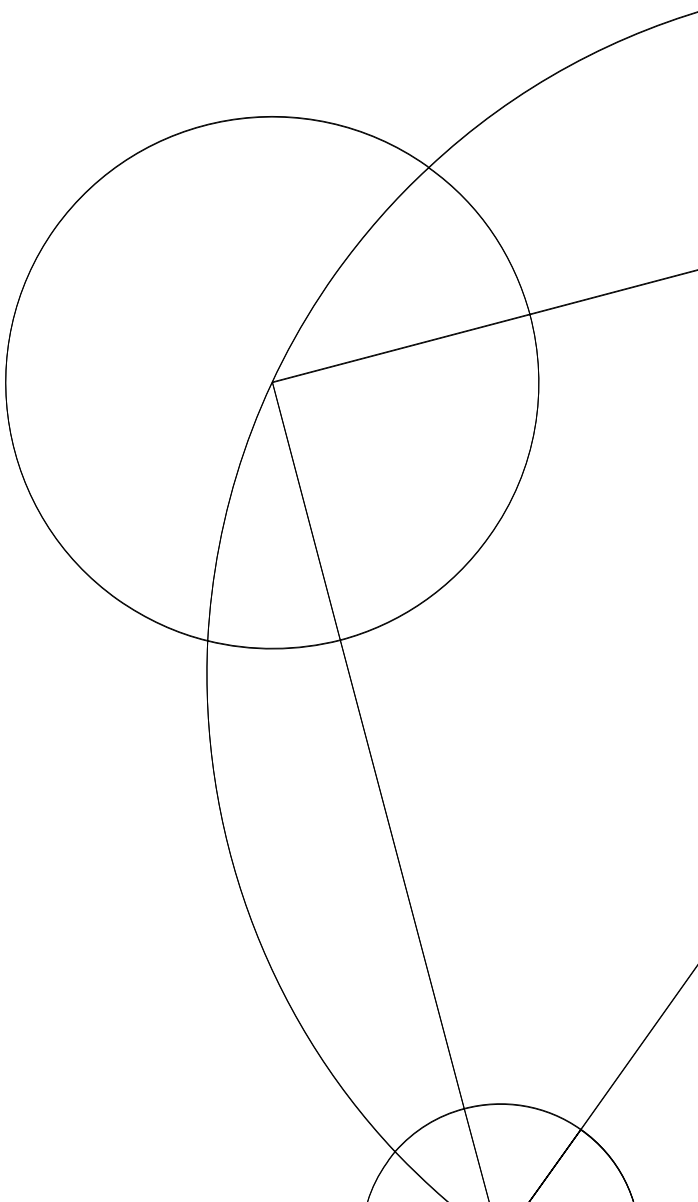

Abstract

Quantum computers has long promised to revolutionise the way we view information. However, the superconducting qubits commonly touted by the big technology companies have always suffered from debilitating errors. To remedy this, many have turned to reducing the sources of errors, but few have considered reducing the qubit's sensitivity instead. This complementary approach was recently attributed with helping the fluxonium achieve its sudden leap forward in coherence times. However, the question then arises if we can achieve the same insensitivity or protection in other qubits.

In this thesis, we investigate the $\hat{n}$-parity protected qubit, which uses a π-periodic Josephson element to achieve similar protection against $\hat{n}$ relaxation, while distinctively remaining in the integer number of Cooper pairs regime. We introduce how this π-periodic Josephson element can be achieved in SNS junctions, and document the ongoing process of realising such a protected qubit in a scalable 2DEG platform.

Acknowledgements

To Charlie, for giving me the opportunity to work in his group and to explore a new sphere of physics which I had little background, but much interest in.

To Albert and Laurits, for welcoming me into the group and teaching me everything I know about nanofabrication today.

To Jose and Oscar, for working on the $\hat{n}$-parity qubit and soldiering through all the early fab problems together with me.

And to the rest of the gatemon group – past and present – for the many interesting journal clubs, useful fabrication and measurement advice, and the friendship.

Contents

List of Figures

1 Introduction

1.1 Motivation

Quantum computing is a new paradigm of information processing where data is encoded and manipulated as quantum bits (qubits) instead of classical ones. This migration to the quantum world, throws open the doors for discovery of fundamentally new information processing techniques that exploit uniquely quantum phenomena. For example, machine learning applications could be trained by variationally entangling quantum circuits, instead of tuning classical variables [1]. Or, complex systems with underlying quantum interactions could be more naturally and efficiently simulated on similarly quantum computers over classical ones [2]. However, further progress in executing ever more sophisticated quantum algorithms is currently still greatly hampered by the inadequacies of modern quantum hardware.

One of these inadequacies is the spontaneous relaxation of qubits, which remains one of the major problems of superconducting qubits today. These relaxation errors occur because of decay channels in the environment which couple the qubit's $|0\rangle$ and $|1\rangle$ states, encouraging it to relax into the lower energy state and destroying the encoded information in the process. The reason this plagues superconducting qubits in particular, is the double whammy of (i) their strong coupling to (ii) a multitude of very dense decay channels, à la Fermi's golden rule [3]. Great strides have been made in reducing the density of some of these decay channels: via Bogoliubov quasiparticle traps, Purcell filters, three-dimensional cavities, and so on [4–6]. However, there is also the complementary approach of reducing the qubit's coupling to these decay channels, which has not seen as much experimental progress and attention – until recently.

This decoupling to the decay channels is primarily achieved by designing so-called protected qubits, which have states with reduced overlap relative to a specific decay channel's operator $\langle 0|\hat{O}|1\rangle$. Current experimental efforts are mainly focused on minimising these overlaps with respect to the natural $\hat{n}, \hat{\varphi}$ operators; translating to protection against decay channels such as relaxation into charge defects in the qubit's environment. The practical value of this $\hat{n}, \hat{\varphi}$ protection can perhaps most prominently been seen in the recent millisecond coherence fluxonium paper, where such a protection was attributed with helping achieve the ten-fold leap in coherence time over the previous long-standing record [7, 8].

1.2 Background

However, the fluxonium is not the only qubit which can achieve this $\hat{n}, \hat{\varphi}$ protection. It is also possible to create a similarly protected qubit which preserves the integer discreteness of $\hat{n}$ and 2π periodicity of $\hat{\varphi}$ from the microscopic picture of superconductivity. This qubit takes the general form of a capacitively-shunted π-periodic Josephson-like element, which would host non-overlapping states that differ in the parity of $\hat{n}$, as sketched in figure 1.1.

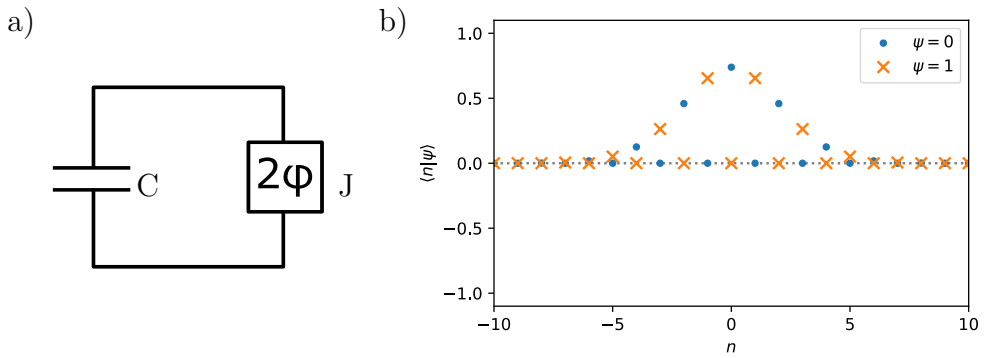

Figure 1.1: a) Circuit diagram and b) $\hat{n}$ wavefunction of a $\hat{n}$-parity qubit

The first attempt at such a $\hat{n}$-parity qubit was based on the Josephson rhombus; first dreamt up in the context of lattice codes, and later applied to the simpler qubit [9–11]. These rhombuses require four strictly identical Josephson junctions, since it is this symmetry that provides the desired $\cos(2\varphi)$ energy dependence under frustration. However, perfectly identical junctions are hard to fabricate, and this first attempt still had residual 2π-periodic components which would have limited its $\hat{n}$ protection [11].

An alternative approach is to use superconductor-semiconductor junctions, which have two separate benefits. Firstly, such junctions would be tunable via electrostatic gates, which would help in balancing them without interfering with flux-biasing of the rhombus itself. Secondly, these junctions also have non-sinusoidal energy dependence, with higher harmonics that can be directly interfered to yield a π-periodic element using only two junctions.

Such a superconductor-semiconductor $\hat{n}$-parity qubit was previously attempted in our lab [12]. However, it could not be operated in the perfectly π-periodic regime either, for the distinct reason that the qubit could not be tracked that deep into the protected regime. Additionally, these junctions were made using VLS (vapour-liquid-solid) nanowires, which had to be manually picked and placed on the chip, and thus wasn't readily scalable to multiple qubits should the desire arise in the future.

1.3 Outline of Thesis

In this thesis, we set out to build upon the aforementioned superconductor-semiconductor $\hat{n}$-parity qubit – by first migrating it to the more scalable 2DEG (2D electron gas) platform used by other devices in our lab. This migration is currently still ongoing, but we will describe the envisaged 2DEG $\hat{n}$-parity qubit and give a summary of the progress thus far. Additionally, we will also provide a longer-form and more explicit introduction to SNS junctions. Using a harmonic interpretation of the its Josephson energy, we can directly compare the transmon, gatemon and $\hat{n}$-parity qubit via the respective SIS junction, SNS junction, and π-periodic SNS SQUID.

The remainder of this thesis will be organised as follows. We will start in chapter 2 with a crash course on conventional superconducting qubits; building up to the archetypical transmon which we will show is not $\hat{n}$ protected. Subsequently in chapter 3, we will discuss the SNS junction and show how the harmonic interpretation allows us to understand and compare the various integer n qubit variants. In chapter 4, we will introduce the 2DEG material platform used and provide an overview of the fabrication process. Chapter 5 will present measurements done on a single-junction gatemon, which gives us a first look at the SNS junctions which would eventually go into the $\hat{n}$-parity qubit. Finally, in chapter 6 we will show how the 2DEG $\hat{n}$-parity qubit is expected to look like, and summarise our progress thus far.

2 Basics of Superconducting Circuits

2.1 Canonical Quantisation of Electrical Circuits

The energy stored in any non-dissipative electrical lumped element is

$$H = \int IV \; dt \tag{2.1}$$

where I and V are the current and voltage across the element, and t is time. Thus, it follows that in the formulation of Hamiltonian mechanics, the generalised positions and conjugate momentums of such a conservative electrical circuit would be the negative charge $-Q$ and node flux Φ respectively, defined at each node in the circuit as

$$-Q = -\int I \; dt \tag{2.2}$$

$$\Phi = \int V \; dt \tag{2.3}$$

The above can be proven by checking its consistency with Hamilton's equations,

$$\frac{\partial H}{\partial(-Q)} = -\frac{\partial H/\partial t}{\partial Q/\partial t} = -\frac{IV}{I} = -\frac{d\Phi}{dt} \tag{2.4}$$

$$\frac{\partial H}{\partial \Phi} = \frac{\partial H/\partial t}{\partial \Phi/\partial t} = \frac{IV}{V} = \frac{dQ}{dt} \tag{2.5}$$

Consequently, in moving to quantum mechanics, conservative electrical circuits can be canonically quantised by promoting Q and Φ to canonically conjugate quantum operators, with a commutator of

$$[-\hat{Q}, \hat{\Phi}] = i\hbar \tag{2.6}$$

2.2 SIS Junctions

When a material becomes superconducting, its electrons pair up into Cooper pairs which then condense into a single macroscopic quantum state described by a Ginzburg-Landau wavefunction of [13]

$$\psi = \sqrt{n}e^{i\phi} \tag{2.7}$$

where n is the number of Cooper pairs, and ϕ is the superconducting phase. This distinctive behaviour allows for new electrical elements to be realised; most common of which is the SIS Josephson junction [14]. Such a junction consists of two superconducting leads S separated by a thin insulating barrier I. For example, many superconducting qubits use Al/AlO_x in the geometry sketched in figure 2.1 to form a SIS junction.

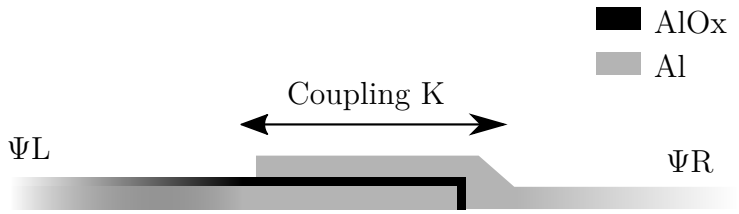

Figure 2.1: Cross-section of a Al/AlO_x Josephson tunnelling junction

The weak insulating barrier allows for some coupling between the wavefunctions of each superconductor. This can be modelled as a coupling element K in the Hamiltonian of the junction, which results in the following Schrödinger equation [15]

$$i\hbar\frac{\partial}{\partial t}\begin{pmatrix}\psi_L\\ \psi_R\end{pmatrix} = \begin{pmatrix}0 & K\\ K & -2eV\end{pmatrix}\begin{pmatrix}\psi_L\\ \psi_R\end{pmatrix} \tag{2.8}$$

where $\psi_{L/R} = \sqrt{n_{L/R}}e^{i\phi_{L/R}}$ is the Ginzburg-Landau wavefunction of the left/right superconductor, K is the coupling element, and V is potential difference across the junction. Solving equation 2.8 and separating the real and imaginary components yields the Josephson equations

$$\frac{\partial\varphi}{\partial t} \coloneqq \frac{\partial}{\partial t}(\phi_R - \phi_L) = \frac{2eV}{\hbar} \tag{2.9}$$

$$I = -2e\frac{\partial n_L}{\partial t} = -2e\sqrt{n_L n_R}\frac{2K}{\hbar}\sin(\varphi) \coloneqq I_c\sin(\varphi) \tag{2.10}$$

where φ is the superconducting phase difference, I the current, and I_c the critical current of the junction. The energy stored in the junction can then be calculated to be

$$U = \int I_c\sin(\varphi)\frac{\hbar}{2e}\frac{\partial\varphi}{\partial t}\,dt = -\frac{\hbar I_c}{2e}\cos(\varphi) \tag{2.11}$$

The last thing to note here is that $n = Q/(-2e)$, and $\varphi = 2e\Phi/\hbar$ from equation 2.3 and 2.9. Thus, they can also be promoted to canonically conjugate quantum operators following section 2.1, up to a constant factor. Additionally, $\hat{n}$ and $\hat{\varphi}$ turns out to be less cumbersome for all our subsequent analysis. Thus, we will switch over exclusively to them, with their commutator modified from equation 2.6 to be

$$[\hat{n}, \hat{\varphi}] = i \tag{2.12}$$

2.3 Capacitively Shunted SIS Junction

To create a superconducting qubit, we can shunt a Josephson junction J with a capacitance C, as depicted in figure 2.2. This capacitance arises naturally between the electrical planes of each of the two superconducting leads. However, there are typically also environmental charges which can also couple differentially to each of these planes, which we model as a offset voltage source V_g and capacitance C_g.

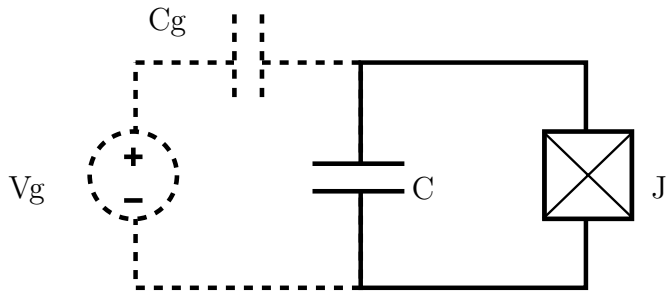

Figure 2.2: Circuit diagram of a capacitively shunted Josephson junction
(The dotted lines denote stray charges in the environment unintentionally coupling to the circuit)

For an SIS junction, the Hamiltonian of such a circuit can be written down as [3]

$$\begin{aligned}\hat{H} &= \frac{(2e)^2}{2C}\left(\hat{n} - \frac{C_g V_g}{2e}\right)^2 - \frac{\hbar I_c}{2e}\cos(\hat{\varphi}) \\ &\coloneqq 4E_C(\hat{n} - n_g)^2 - E_J\cos(\hat{\varphi})\end{aligned} \tag{2.13}$$

where $E_C = e^2/2C$ is the charging energy of the capacitor, $E_J = \hbar I_c/2e$ is the Josephson energy of the junction, and $n_g = C_g V_g/2e$ is the offset charge due to the environment. To find the eigenstates, we can rewrite $\hat{H}$ exclusively in terms of $\hat{n}$ or $\hat{\varphi}$ to get

$$\begin{aligned}\hat{H} &= 4E_C\left(i\frac{\partial}{\partial\varphi} - n_g\right)^2 - E_J\cos(\hat{\varphi}) \\ &= 4E_C\left(\hat{n} - n_g\right)^2 - \frac{E_J}{2}\left(|n+1\rangle\langle n| + |n\rangle\langle n+1|\right)\end{aligned} \tag{2.14}$$

where $\langle n|\hat{n}|n\rangle = n$. The $\hat{\varphi}$ version is related to Matthieu's differential equation, and thus has known eigenenergies and eigenfunctions [3]. The $\hat{n}$ version operates in a discrete basis since $n \in \mathbb{Z}_0$, and thus has a representative matrix that can be truncated and numerically diagonalised. We do the latter for a range of different parameters and plot the results in figure 2.3.

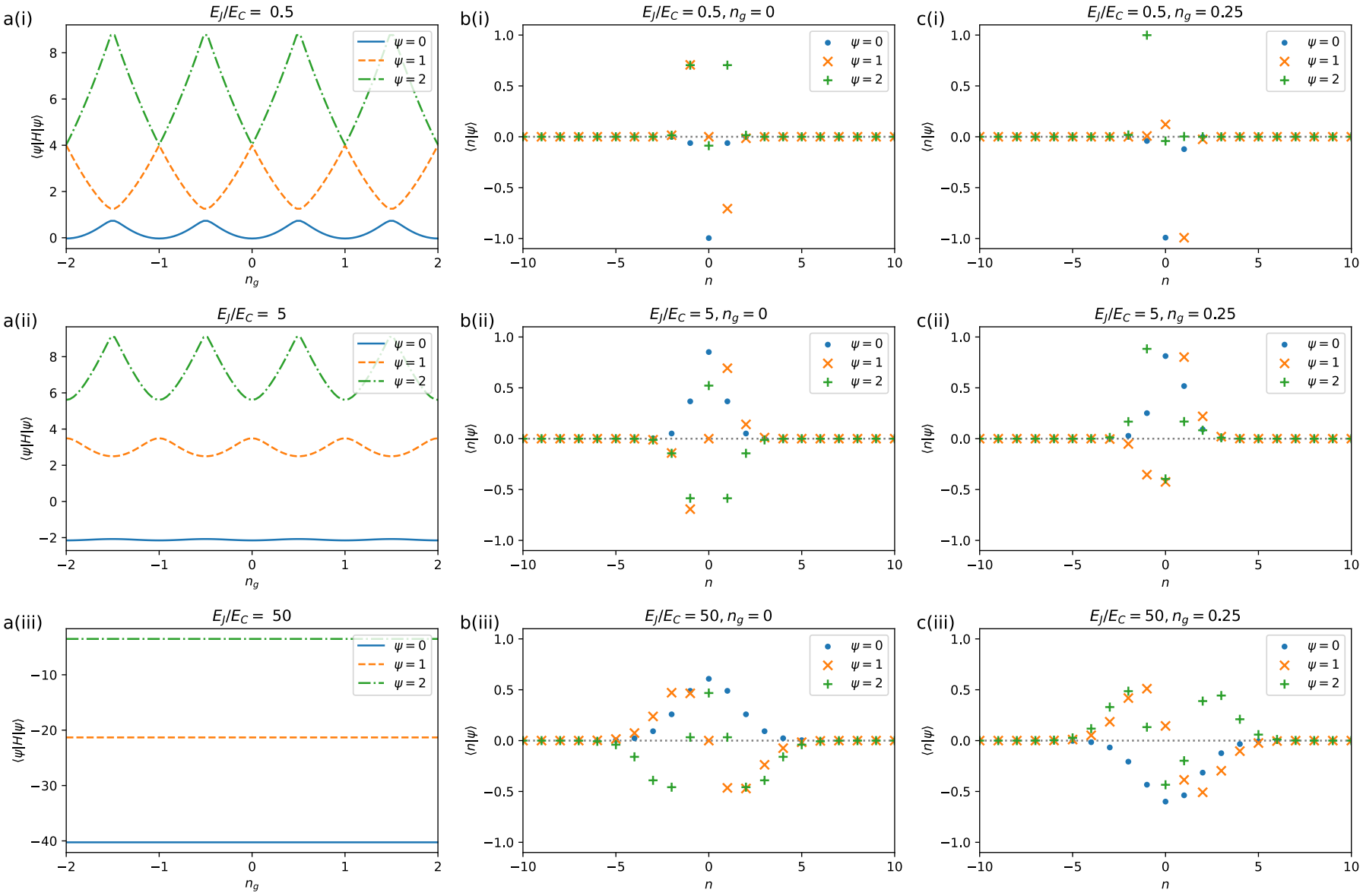

Figure 2.3: (a) Charge dispersion, and wavefunctions at (b) $n_g = 0$ (c) $n_g = 0.25$ of a capacitively-shunted SIS junction for $E_J/E_C =$ (i) 0.5, (ii) 5, (iii) 50

From figure 2.3a, we can observe that the circuit has unequally-spaced energy levels, and thus can be used as qubits. Additionally, as E_J/E_C increases, these energy levels becomes less sensitive to variations in n_g, but they also become more equally-spaced. The former is beneficial for quantum computation, since a stable qubit energy prevents dephasing errors. The latter is detrimental, since it results in more leakage errors and/or longer gate times. However, there have been theoretical and experimental evidence suggesting that the benefits outweigh the cost [3, 16]. As a result, this large E_J/E_C regime has become widely adopted, with such qubits named transmons.

Each of these energy levels also have their associated wavefunctions plotted in figure 2.3b and 2.3c, where they can be observed to alternate between having odd and even envelopes about $n = n_g$. This behaviour means that twice-adjacent energy levels will always have zero $\langle\psi_i|\hat{n}|\psi_{i+2}\rangle$ overlap at half-integer n_g due to their similar oddness or evenness. At non-half-integer n_g, the overlap of twice-adjacent levels becomes less straightforward to determine, since the n discretisation does not occur symmetrically and the resulting wavefunctions are not perfectly odd/even, as can be seen on careful inspection of figure 2.3c(ii) and 2.3c(iii). However, once-adjacent energy levels – on which qubits are typically defined – have non-zero $\langle\psi_i|\hat{n}|\psi_{i+1}\rangle$ overlap at all n_g due to their opposing oddness/evenness. This leads to non-zero $\langle 0|\hat{n}|1\rangle$ overlap in the qubit which would encourage energy relaxation via channels coupled through $\hat{n}$ according to Fermi's golden rule, and such qubits are effectively unprotected against $\hat{n}$ relaxation.

2.4 Transmons

As mentioned before, transmons with $E_J/E_C \gtrsim 50$ have not only proven to be of practical benefit, but also allows us to make analytic approximations of its energy levels. This is because a dominating E_J term would localise the wavefunctions near $\varphi = 0 \mod 2\pi$. Thus, we can Taylor expand equation 2.13 around $\varphi = 0 \mod 2\pi$ to obtain

$$\hat{H} \approx 4E_C(\hat{n} - n_g)^2 + \frac{E_J}{2}\hat{\varphi}^2 - \frac{E_J}{24}\hat{\varphi}^4 + O(\hat{\varphi}^6) - E_J \tag{2.15}$$

Ignoring the quartic φ^4 and higher-order terms, we can identify the Hamiltonian to be similar to a quantum harmonic oscillator. This motivates us to apply second quantisation to the circuit, using annihilation/creation operators of the form

$$\hat{a} = \sqrt[4]{\frac{2E_C}{E_J}}(\hat{n} - n_g) + i\sqrt[4]{\frac{E_J}{32E_C}}\hat{\varphi} \tag{2.16}$$

The resulting second-quantised version of equation 2.15 will then be

$$\hat{H} \approx \sqrt{8E_CE_J}\left(\hat{a}^\dagger\hat{a} + \frac{1}{2}\right) - \frac{E_C}{12}(\hat{a}^\dagger - \hat{a})^4 - E_J \tag{2.17}$$

This form highlights that adjacent energy levels are almost equally spaced, except for the 3rd (and higher) terms. Specifically, including this 3rd term results in

$$\langle k|\hat{H}|k\rangle \approx \sqrt{8E_C E_J}\left(k+\frac{1}{2}\right) - \frac{E_C}{4}(2k^2+2k+1) - E_J \tag{2.18}$$

$$\langle H\rangle_{k+1} - \langle H\rangle_k \approx \sqrt{8E_C E_J} - E_C(k+1) \tag{2.19}$$

where $|k\rangle$ is the k-th excited state, and $\langle k|\hat{H}|k\rangle = \langle H\rangle_k$ is its energy. Thus, the first $|0\rangle \to |1\rangle$ transition will have a energy of $\sqrt{8E_C E_J} - E_C$, and the second $|1\rangle \to |2\rangle$ will an energy lower by E_C. This difference between the first and second transition is named the anharmonicity α, and for the Transmon it takes the approximate value of $\alpha \approx -E_C$.

3 Superconductor-Semiconductor Qubits

3.1 SNS Junction

A close relative of the SIS junction is the SNS junction, which replaces the insulating barrier I with one made from a normal metal N. This allows for Andreev reflection to occur at each N-S interface, where an electron incident from the normal region drags another suitable electron with it to form a Cooper pair in the superconductor, leaving a retroreflected hole in the normal metal as illustrated in figure 3.1 [17].

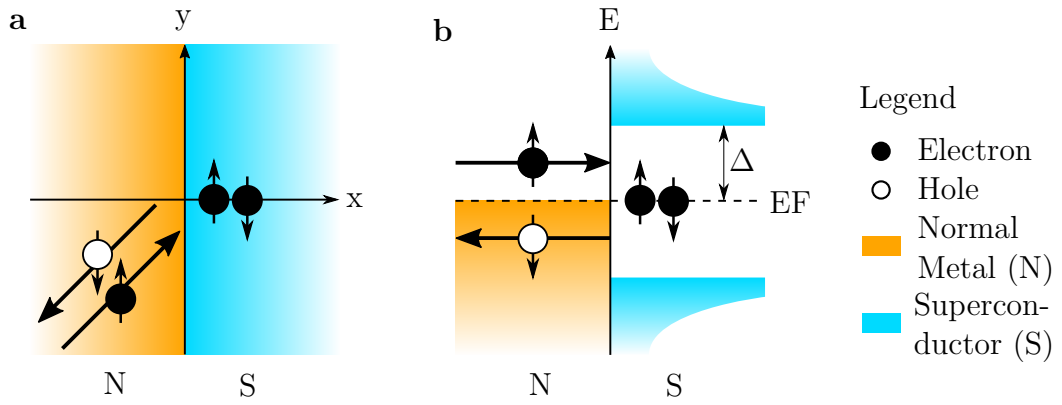

Figure 3.1: Illustration of Andreev reflection in a) spatial coordinates b) energy levels

This allows SNS junctions to host bound states, corresponding to the infinite loop where an electron in the normal metal is reflected as a hole from one N-S interface, and then reflected back to the original electron again at the other interface. These Andreev bound states also carries supercurrents, since the aforementioned process entails Cooper pairs being created in one superconducting lead and annihilated in the other.

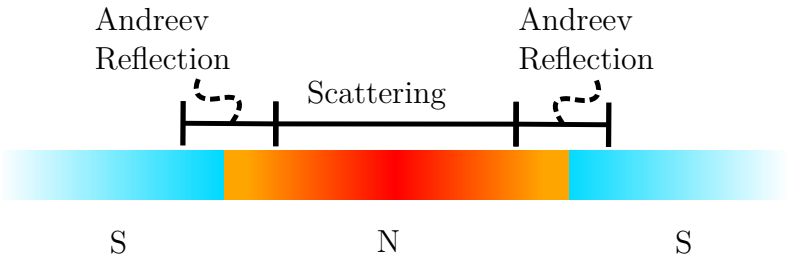

Figure 3.2: SNS junction model, with ideal S-N interfaces separate from the bulk metal

There are several ways to quantitatively model these SNS junctions and their Andreev bound states. However, past work on similar junctions in our lab suggests that ours can be modelled as described in [18], with effectively ideal S-N interfaces separate from the bulk normal metal where scattering might still occur, as sketched in figure 3.2.

These perfect S-N interfaces are assumed to have (i) no mismatch in Fermi velocities (ii) a step-like change in the pairing potentials (iii) no interfacial potential barriers [19, 20]. Matching the wavefunctions supported by the Bogoliubov-de Gennes equation in each region then predicts that Andreev reflection will always occur for electrons and holes under the superconducting gap, with a net phase shift of [19–21]

$$\begin{aligned} |e_i\rangle &\to e^{-i\arccos(E/\Delta)} e^{-i\phi} |h_r\rangle \\ |h_i\rangle &\to e^{-i\arccos(E/\Delta)} e^{i\phi} |e_r\rangle \end{aligned} \tag{3.1}$$

where $|e_i\rangle, |h_i\rangle$ are the incident electron or hole, E its energy, Δ the superconducting gap, ϕ the superconducting phase, and $|e_r\rangle, |h_r\rangle$ the retro-reflected electron or hole. The Andreev bound states can then be found by noting that they should be invariant under the combined Andreev reflection and scattering in the bulk metal. For one-dimensional junctions shorter than the superconducting coherence length ($L < \xi$), these bound states are calculated to have energies of [18, 21]

$$E = \pm\Delta\sqrt{1 - T\sin^2(\varphi/2)} \tag{3.2}$$

where Δ is the superconducting gap, T is the transmission coefficient through the bulk normal metal, and φ is the superconducting phase difference between the two leads. In actual SNS junctions, we expect to see several such one-dimensional channels, each with their own transmission coefficient and Andreev bound states. Their energies have also been empirically observed to vary when gated with a nearby electrostatic gate [22].

In the context of qubits, these SNS junctions would usually be operated at low temperatures and voltages. Thus, we expect that only bound states with negative energies will be filled. This would translate to a total energy stored in the junction of

$$U_J(\varphi) = -\Delta\sum_i \sqrt{1 - T_i\sin^2(\varphi/2)} \tag{3.3}$$

where i is the index of each one-dimensional conduction channel, and T_i its transmission coefficient. The superconducting leads are assumed to be homogeneous, and thus the superconducting gap Δ and phase difference φ should to be the same across all channels.

3.2 SNS Josephson Energy

This SNS Josephson energy (equation 3.3) underlies our ability to create the $\hat{n}$-parity qubit. It is similar to the SIS junction in that both are 2π-periodic in φ. However, the SIS's energy has a purely sinusoidal relation with φ, while the SNS junction can have a much more complex energy dependence as shown in figure 3.3a(i).

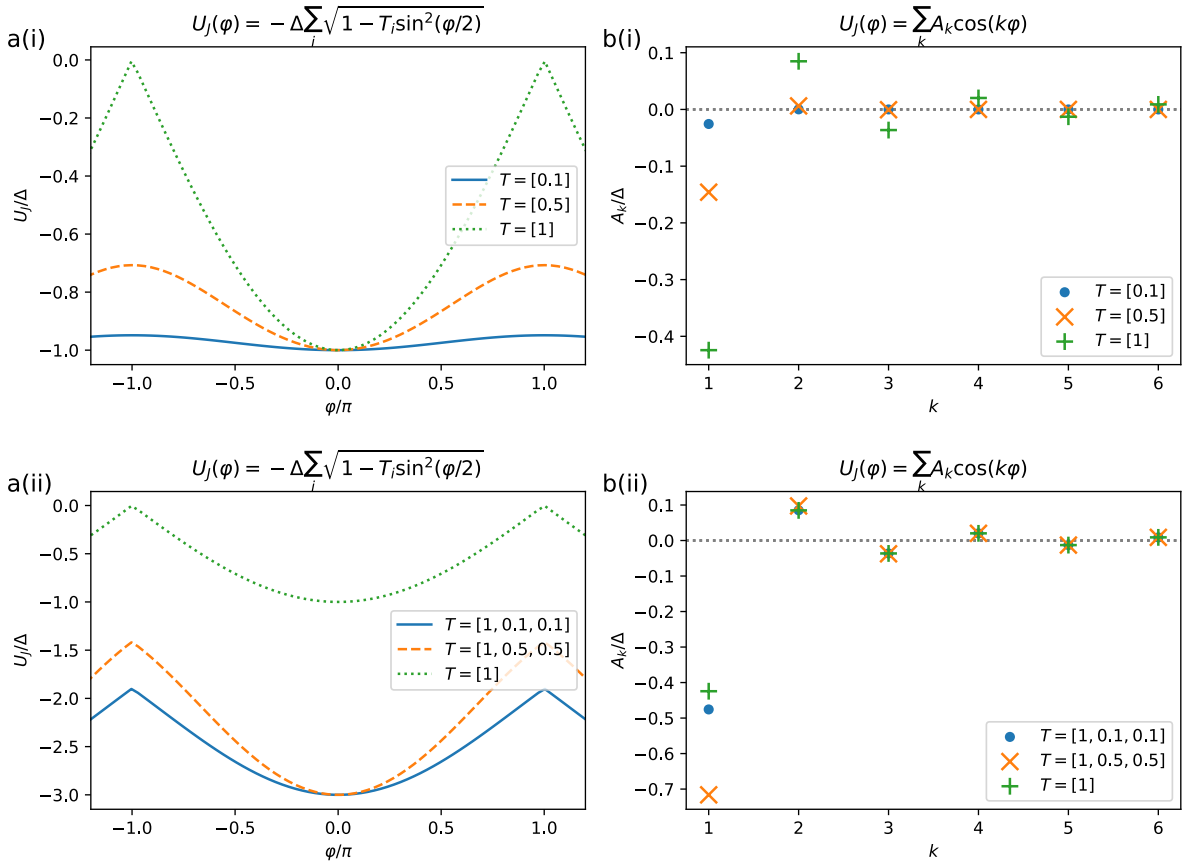

Figure 3.3: SNS junction energy in terms of (a) φ, and (b) harmonics of $\cos(k\varphi)$

To gain further insight into this difference between SIS and SNS junctions, it is useful to decompose the energies into their harmonic components. SIS junctions are purely sinusoidal and thus only has its 1st harmonic. Conversely, SNS junctions can possesses significant higher harmonic components, as encapsulated in

$$U_J(\varphi) = -\sum_k A_k \cos(k\varphi) \tag{3.4}$$

where k denotes the k-th harmonic, A_k is its amplitude, and the use of cosine justified by the evenness of U_J. Since there is only one fundamental frequency, we can cleanly isolate each harmonic and extract its amplitude by beating it with an similar tone, following

$$A_k = \begin{cases} \dfrac{1}{2\pi}\displaystyle\int_{-\pi}^{\pi} E_J(\varphi)\cos(k\varphi)\ d\varphi & \text{for } k = 0 \\ \dfrac{1}{\pi}\displaystyle\int_{-\pi}^{\pi} E_J(\varphi)\cos(k\varphi)\ d\varphi & \text{for } k > 0 \end{cases} \tag{3.5}$$

The physical implications of these higher harmonics will become apparent when discussing qubits in the next section. For now, we can numerically extract these harmonic terms, and compare them across a range of different conduction channels as plotted in figure 3.3b.

For the single channel case in figure 3.3b(i), we can see that high transmission channels have significant higher harmonics, which result in junctions very distinct from the SIS ones. This distinction fades away at middling transmissions, as the higher harmonics vanishes more quickly, causing the 1st harmonic to eventually dominate. However, dropping to even lower transmissions causes the 1st harmonic to also die out, effectively preventing any supercurrent flow across the junction.

In the case of multiple conduction channels, figure 3.3b(ii) reveals that the harmonics of each conduction channel simply sums up. Each conduction channel just adds its own timbre to the choir that is the junction. Thus, adding more lower transmission channels do not diminish the higher harmonics in an absolute sense. However, adding middling transmission channels does disproportionately add to the 1st harmonic, which might end up masking the effect of the higher harmonics in situations like the gatemon. On the other hand, near-zero transmission channels simply adds an offset to the energy of the junction, and are otherwise inconsequential to the behaviour of the junction and any qubit it forms.

3.3 Gatemons

To illustrate the physical implications of the aforementioned higher harmonics, and to inform our later interpretation of the our gatemon measurements, we can look at the capacitively-shunted SNS junction. Analogously to section 2.3, such a circuit will have a Hamiltonian of

$$\begin{aligned} \hat{H} &= 4E_C(\hat{n} - n_g)^2 - \Delta\sum_i \sqrt{1 - T_i \sin^2(\varphi/2)} \\ &= 4E_C(\hat{n} - n_g)^2 - \sum_k A_k \cos(k\varphi) \\ &= 4E_C(\hat{n} - n_g)^2 - \sum_k \frac{A_k}{2}(|n+k\rangle\langle n| + |n\rangle\langle n+k|) \end{aligned} \tag{3.6}$$

where $E_C = e^2/2C$ is the charging energy of the capacitor, n_g the offset charge due

to the environment, Δ the superconducting gap, T_i the transmission coefficient of each conduction channel, and A_k the harmonic coefficients as discussed in section 3.2. Here, it becomes explicit that the higher harmonics of the SNS junction causes it to also couple states that differ by more than one Cooper pair. For the specific case of the capacitively-shunted SNS junction, we would expect this extra coupling to affect the scaling of the charge dispersion and anharmonicity of the qubit.

To quantify the latter, we can restrict ourselves to the so-called gatemon regime of $\varphi \approx 0 \mod 2\pi$, analogous to the transmon regime. Taylor expansion of the SNS Josephson energy in equation 3.3 in this regime would then yield

$$\begin{aligned}\hat{H} &= 4E_C(\hat{n}-n_g)^2 - \Delta\sum_i\left[1+\frac{T_i}{4}\frac{\hat{\varphi}^2}{2}+\left(\frac{T_i}{4}-\frac{3T_i^2}{16}\right)\frac{\varphi^4}{24}+O(\hat{\varphi}^6)\right] \\ &\approx 4E_C(\hat{n}-n_g)^2 - \left(\frac{\Delta}{4}\sum_i T_i\right)\frac{\hat{\varphi}^2}{2}+\left(1-\frac{3\sum_i T_i^2}{4\sum T_i}\right)\left(\frac{\Delta}{4}\sum_i T_i\right)\frac{\varphi^4}{24}-\Delta\sum_i 1\end{aligned} \tag{3.7}$$

This is similar to the transmon version in equation 2.15, except for the substitution of $E_J \to \frac{\Delta}{4}\sum_i T_i$ and an extra coefficient in the quartic φ^4 term. Thus, in the same vein as equation 2.17, the gatemon would have an approximate second quantised Hamiltonian of

$$\hat{H} \approx \sqrt{2E_C\Delta\sum_i T_i}\left(\hat{a}^\dagger\hat{a}+\frac{1}{2}\right)-\left(1-\frac{3\sum_i T_i^2}{4\sum T_i}\right)\frac{E_C}{2}(\hat{a}^\dagger-\hat{a})^4-\Delta\sum_i 1 \tag{3.8}$$

where $\hat{a}, \hat{a}^\dagger$ are creation/annihilation operators of the gatemon. Analogously to equation 2.19, This Hamiltonian will yield transition frequencies and associated anharmonicity of the gatemon of

$$\langle H\rangle_{k+1} - \langle H\rangle_k \approx \sqrt{2E_C\Delta\sum_i T_i}-\left(1-\frac{3\sum_i T_i^2}{4\sum T_i}\right)E_C(k+1) \tag{3.9}$$

where $\langle H\rangle_k = \langle k|H|k\rangle$ is the energy of the k-th state of the gatemon. Thus, it can be seen that a SNS junction with mostly high transmission channels would have $\alpha = -E_C/4$. while one with mostly low transmission channels would have $\alpha = -E_C$.

3.4 $\hat{n}$-Parity Protected Qubits

We are now ready to introduce the $\hat{n}$-parity protected qubit, which is just a SQUID loop of two identical SNS junctions, biased at half-flux-quantum and shunted by a capacitor, as sketched in figure 3.4.

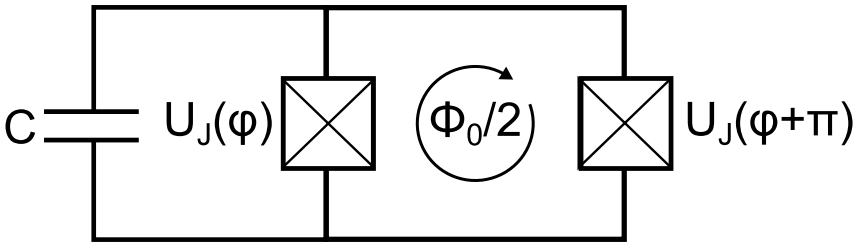

Figure 3.4: Circuit diagram of a $\hat{n}$-parity qubit, using identical SNS junctions

At first glance, it just looks like a symmetric flux-tunable transmon. However, the crucial difference is in the SNS junctions used and their higher harmonics. The biasing at half-flux quantum causes all the odd harmonics to destructively interfere in the SQUID, leaving just the even harmonics according to

$$\begin{aligned} U_J(\varphi) + U_J(\varphi+\pi) &= \left\{ \begin{array}{l} \displaystyle\sum_{k\in\text{odd}} [A_k \cos(k\varphi) + A_k \cos(k\varphi+\pi)] \\ \displaystyle + \sum_{k\in\text{even}} [A_k \cos(k\varphi) + A_k \cos(k\varphi+2\pi)] \end{array} \right\} \\ &= \sum_{k\in\text{even}} 2A_k \cos(k\varphi) \end{aligned} \tag{3.10}$$

where U_J is the energy of a single SNS junction, and A_k is its harmonic coefficients as discussed in section 3.2. The Josephson energy of such a symmetric, half-integer-biased SNS SQUID loop is plotted for a range of different conduction channels in figure 3.5.

From figure 3.5, it can be seen that regardless of whether the the conduction channels are few or numerous, with high or low transmission coefficients; the odd harmonics will always destructively interfere as long as they are of similar in each of the two SNS junctions. High transmission channels only serve to increase the absolute value of these even harmonic coefficients, which might be useful in attaining the offset-charge-insensitive regime of large A_2/E_C like the transmon; but it would not affect the $\hat{n}$ protection.

To illustrate how these even harmonics result in $\hat{n}$ protection, we can write down the full Hamiltonian of the $\hat{n}$-parity qubit circuit sketched in figure 3.4 as

$$\begin{aligned} \hat{H} &= 4E_C(\hat{n}-n_g)^2 - \sum_k 2A_{2k}\cos(2k\varphi) \\ &= 4E_C(\hat{n}-n_g)^2 - \sum_k A_{2k}(|n+2k\rangle\langle n| + |n\rangle\langle n+2k|) \end{aligned} \tag{3.11}$$

where $E_C = e^2/2C$ is the charging energy of the capacitor, n_g the offset charge due to the environment, A_{2k} the even harmonic coefficients, and $\langle n|\hat{n}|n\rangle = n$.

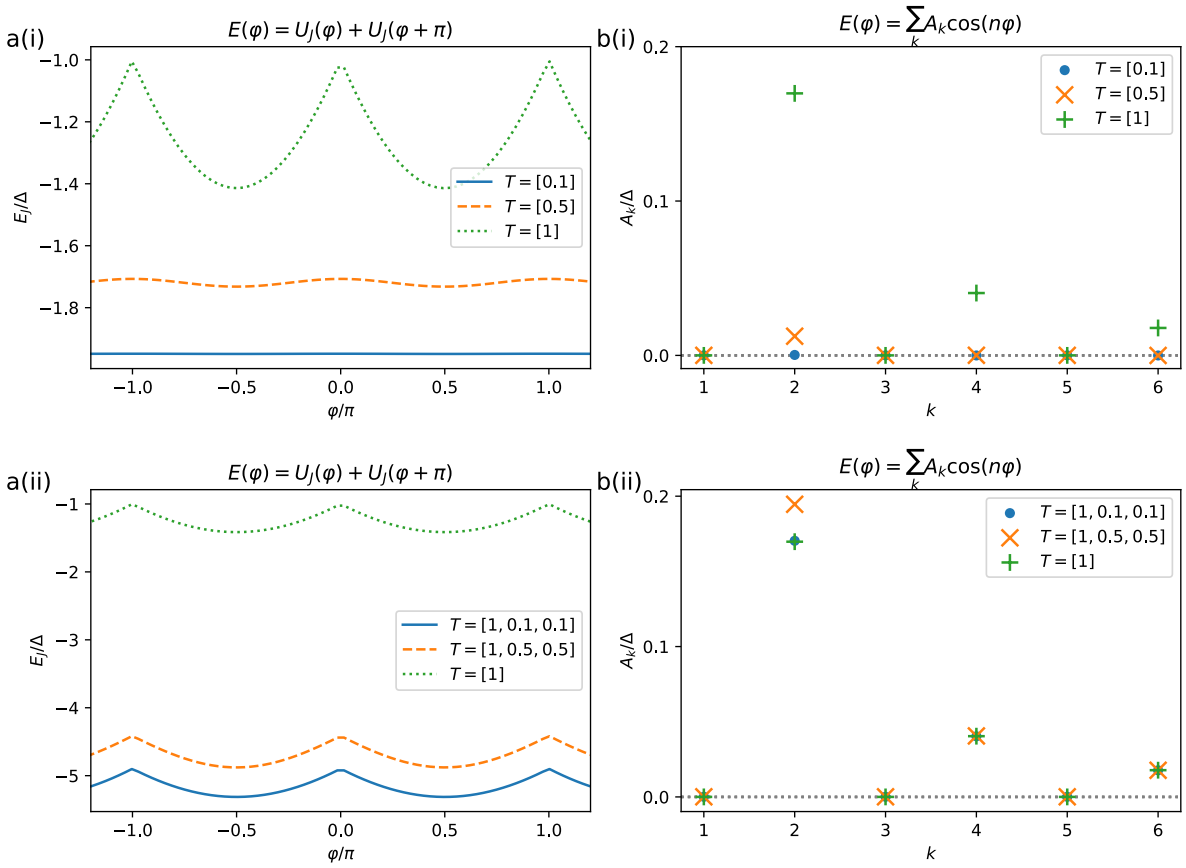

Figure 3.5: $\hat{n}$-parity qubit Josephson energy in terms of (a) φ, and (b) harmonics of $\cos(k\varphi)$

This explicitly shows that the SNS SQUID loop only couples states that differ by an even number of Cooper pairs. As a result, the odd and even n components are internally coupled, but not coupled with each other. Thus, the Hamiltonian will always support two otherwise identical wavefunctions that live in each of the independent odd/even n subspace, with zero $\langle 0|\hat{n}|1\rangle$ overlap between them.

To make this $\hat{n}$-parity separation even more explicit, we can numerically solve for the eigenfunctions of equation 3.11. This can be done via a similar method to figure 2.3: by truncating the n-basis along with any accompanying $|n + 2k\rangle \langle n|$ coupling terms, and then numerical;y diagonalising the matrix. The resulting energy levels and associated wavefunctions – for a junction with a single transparent channel – are plotted in figure 3.6, where the two degenerate wavefunctions with only even/odd n components can be seen.

Additionally, it is noted that in the offset-charge-sensitive regime plotted in figure 3.6a(ii), the energy levels of the two branches are not degenerate. This would allow for easier cQED measurements, eliminating the readout and driving problem experienced in the first generation of the SNS $\hat{n}$-parity qubit.

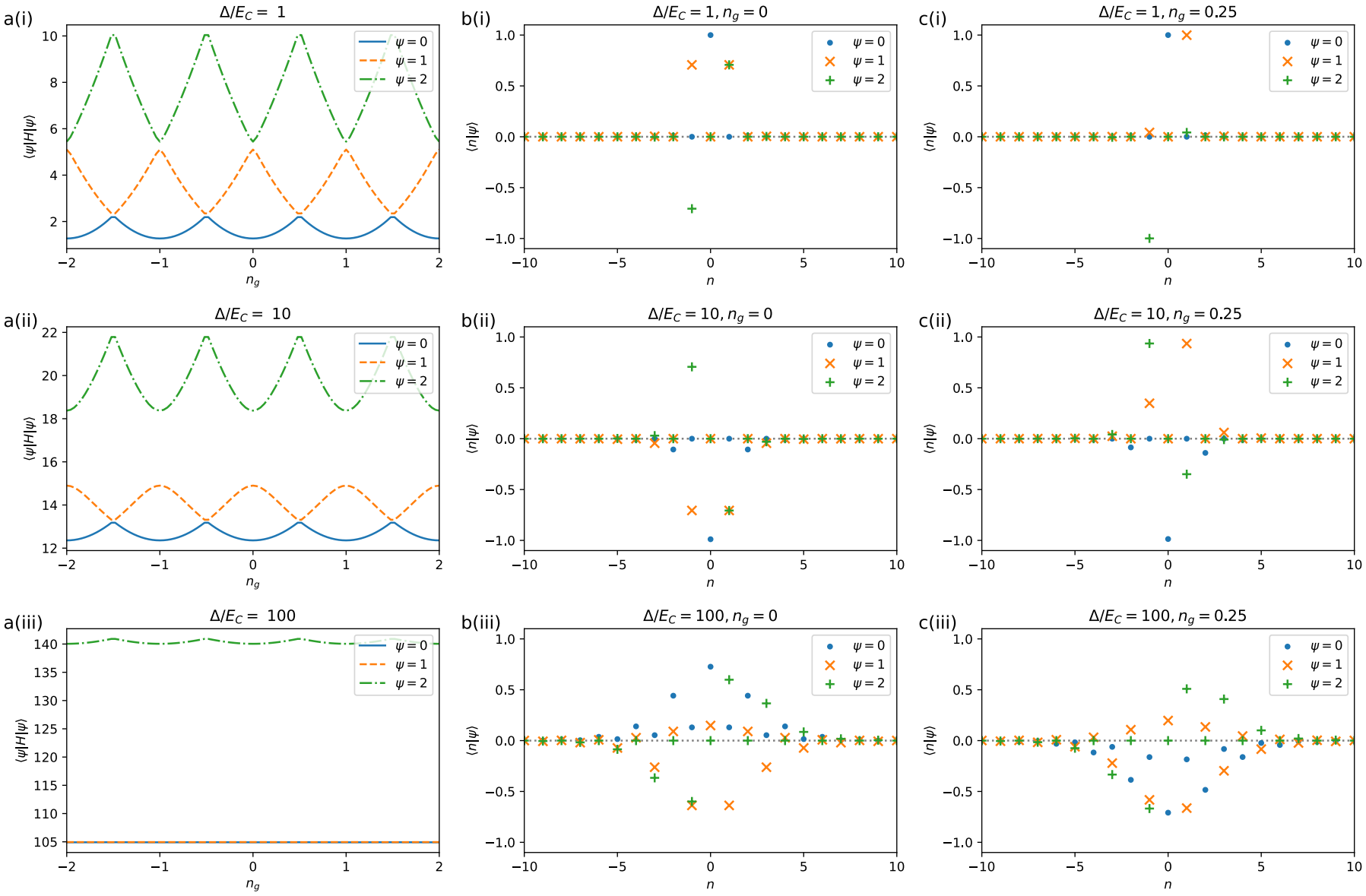

Figure 3.6: (a) Charge dispersion, and wavefunctions at (b) $n_g = 0$ (c) $n_g = 0.25$ of a $\hat{n}$-parity qubit made out of SNS junctions with a single transparent channel for $\Delta/E_C =$ (i) 1, (ii) 10, (iii) 100

4 Nanofabrication

4.1 2DEG Heterostructure

As mentioned in the introduction, we set out to develop the $\hat{n}$-parity qubit by first migrating it to a more scalable 2DEG (2D electron gas) platform. The specific platform we used was grown by the Manfra group at Purdue University, and it consists of an InAs quantum well (yellow), cladded by InGaAs barriers (green), as shown in figure 4.1. This cladded quantum well is grown on an InP wafer (lavender) via a well-optimised buffer heterostructure. Additionally, epitaxial aluminium (grey) was also grown as the last layer, to allows us to use it to form the clean S-N interface required for our junctions.

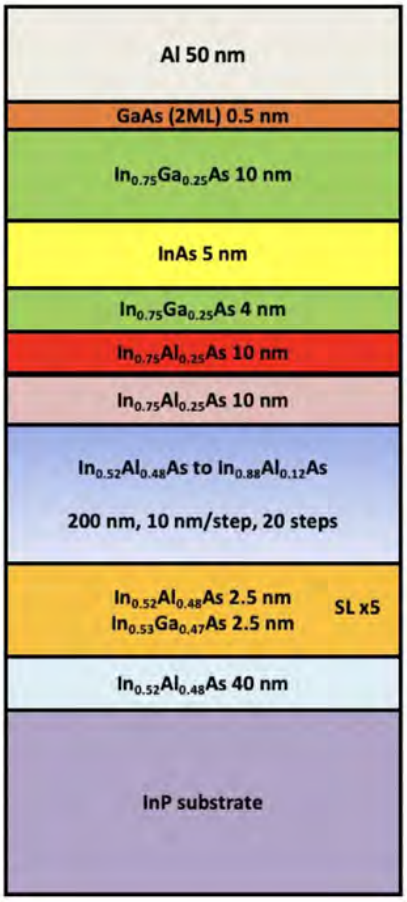

Figure 4.1: Schematic of the 2DEG heterostructure used
(Credits to the Manfra group at Purdue University)

It is also noted that this platform is an enhanced, higher mobility version of the one used in the first 2DEG gatemon reported in [23].

4.2 Fabrication Process

The aforementioned 2DEG heterostructure then had to be integrated with several other electrical elements to form the qubit; elements such as the junction, the capacitor, the gate lines, and so on. In our case, we have continually been developing a fabrication process that can be broken down into six major steps as enumerated below. Figure 4.2 also shows micrographs taken at the end of each of these major step, to provide some visual context.

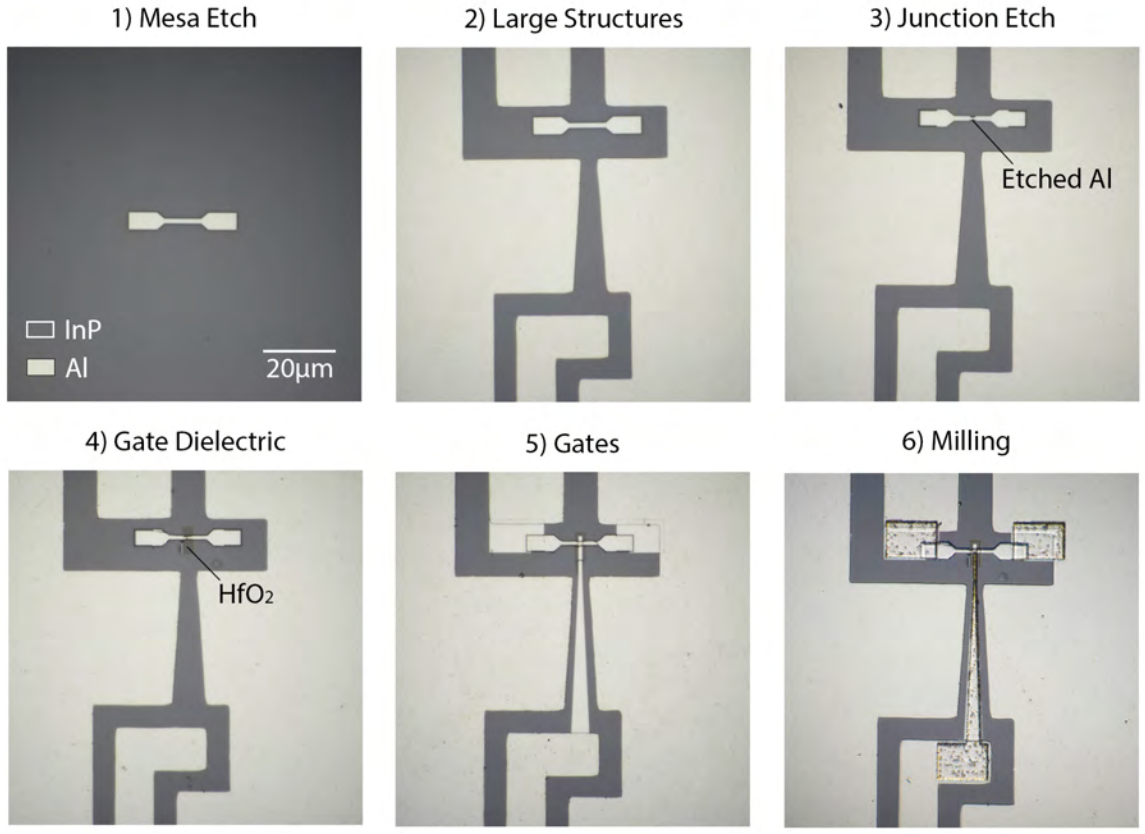

Figure 4.2: Overview of the fabrication process; optical micrographs taken after each major step in the fabrication a gatemon

1) **Mesa Etch:** The first step after scribing out a chip from the wafer, is to etch most of the 2DEG away. This is because although the 2DEG is crucial for realising our SNS junctions, it is also extremely lossy at the microwave frequencies which the qubit will be operating in. Thus, most of the 2DEG has to be removed to minimise any dissipation of the qubit into the substrate. We leave only a few small mesas of 2DEG which will later be used to define the junction, as pictured in figure 4.2.1.

2) **Large Structures:** After etching most of the chip down to the InP substrate, we can start populating it with the larger electrical elements such as the ground

plane, capacitors, and control lines. These elements are all realised by selectively depositing Al in specific geometries. We arbitrarily chose to do this via a lift-off process, and although it is generally reliable, some of the more complex shapes like the coplanar waveguide resonators might require some patience to coax off.

3) **Junction Etch:** Having defined most of the other elements, we turn to focus on the Josephson junction. We define our junction by etching away a stripe of epitaxial Al across the mesa as shown in figure 4.2.3. This creates the two superconducting leads, which have an epitaxial interface with the 2DEG cladding and by extension the 2DEG itself. This is what forms the SNS junction discussed in section 3.1. However, it is noted that the junctions we use are relatively fine at ∼300 nm, and this method does result in noticeable variance in junction length on that fine a scale.

4) **Gate Dielectric:** After the junction has been defined, we work towards covering it with an electrostatic gate. This gate would allow some tuning of the Andreev bound states, as briefly discussed in section 3.1. But before the gate can be deposited, a dielectric has to be inserted to electrically isolate the gate from the superconducting leads of the junction. In our case, we opted to use small HfO_2 strips grown using atomic layer deposition, since it was a widely used process in our lab.

5) **Gates:** The electrostatic gate itself follow next. We initially used a 300 nm thick gate since we were trying to climb the similarly tall mesa with it. The initial motivation for this was to continuously extend the gate a distance away from the junction. This would then allow us to subsequently mill and make electrical contact with the gate far away from the junction, where any resulting defects would have minimal repercussions on the qubit. However, after little luck with that strategy, we have since started to move towards 50 nm thin gates and doing the climbing together with the milling in the next step instead.

6) **Milling**: The last step is to connect all the newly created components together. This electrical connection is ensured by using Ar ion milling to remove any insulating surface oxides, before new Al is deposited over the freshly milled surface to create a galvanic connection. Additionally, this step also has the task of climbing either the mesa or the gate and thus is very thick at 400 nm. Visual inspection of these climbs doesn't reveal any clear signs of discontinuity, as shown in figure 4.3.

The last version of the recipe used is provided in the appendix. It is the same recipe used to produce the working gatemon discussed in chapter 5, and is product passes visual inspection, as shown in figure 4.3. However, it has only been used once and even then there were some minor yield issues with it. Thus, some refinement of the recipe might still be required.

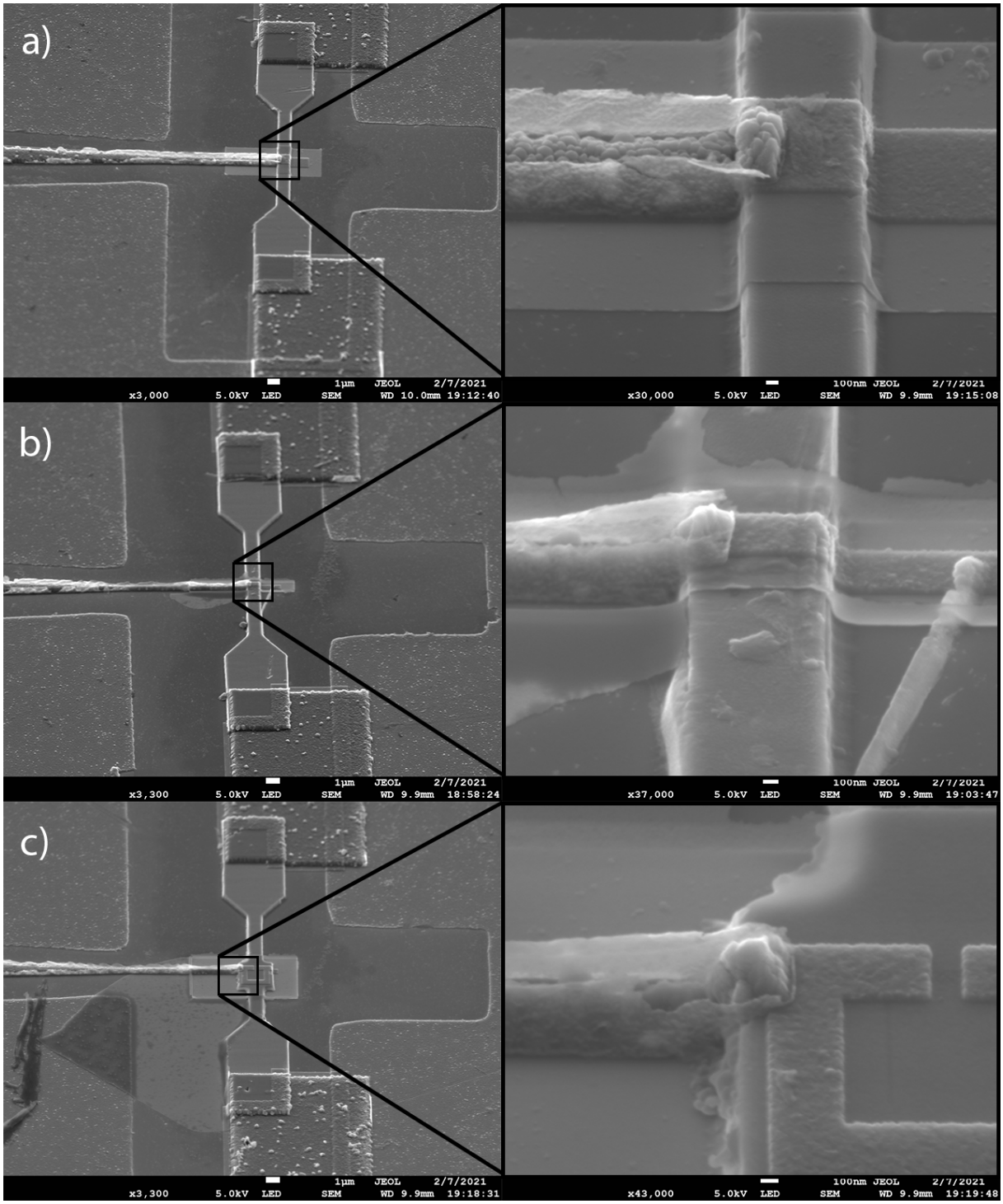

Figure 4.3: SEM micrograph a (a) thick straight (b) thin straight, and (c) C-shaped electrostatic gate climbing up the 2DEG mesas

5 2DEG Gatemon

5.1 Device & Fridge Setup

We tried making a gatemon device to test our fabrication method; to ensure that it could still produce a 2DEG gatemon similar to what was already accomplished in [23]. This took a few tries as we tweaked the fabrication process for some sporadic issues, but we eventually got a nicely fabricated chip as shown in figure 5.1.

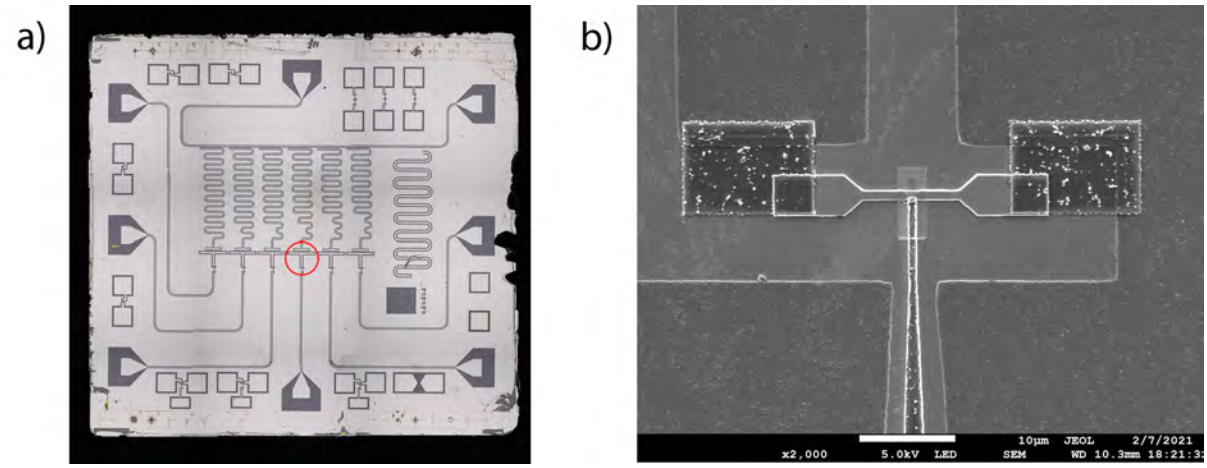

Figure 5.1: (a) Optical micrograph of the chip, with the measured gatemon circled in red, and (b) SEM micrograph of the junction of the same gatemon

This chip had multiple gatemons with a variety of gate designs. However, we ended up focusing mostly on the one gatemon circled in red in figure 5.1a, which corresponded to a simple, straight gate as shown in figure 5.1b. This chip was glued and bonded to the printed circuit board shown in the middle of figure 5.2, which was in turn sandwiched inside the copper sample box shown in the same figure, using Indium seals.

The sample box was then mounted in a cylindrical puck shown in figure 5.3a and 5.3b, which was then finally loaded in the dilution refrigerator shown in figure 5.3c; within the stainless steel cylinder in the middle of the picture. The loaded fridge was then left to thermalise to a base temperature of $\sim$50 mK over a few weeks as the sample was being measured.

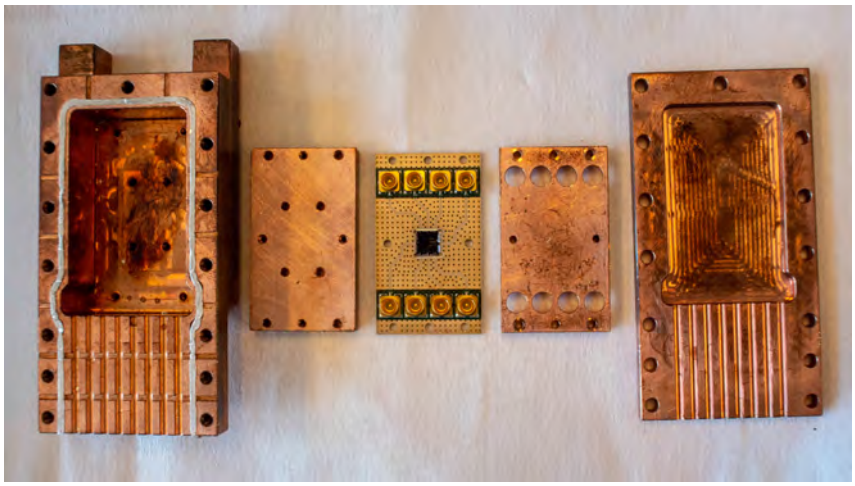

Figure 5.2: Components comprising the sample box

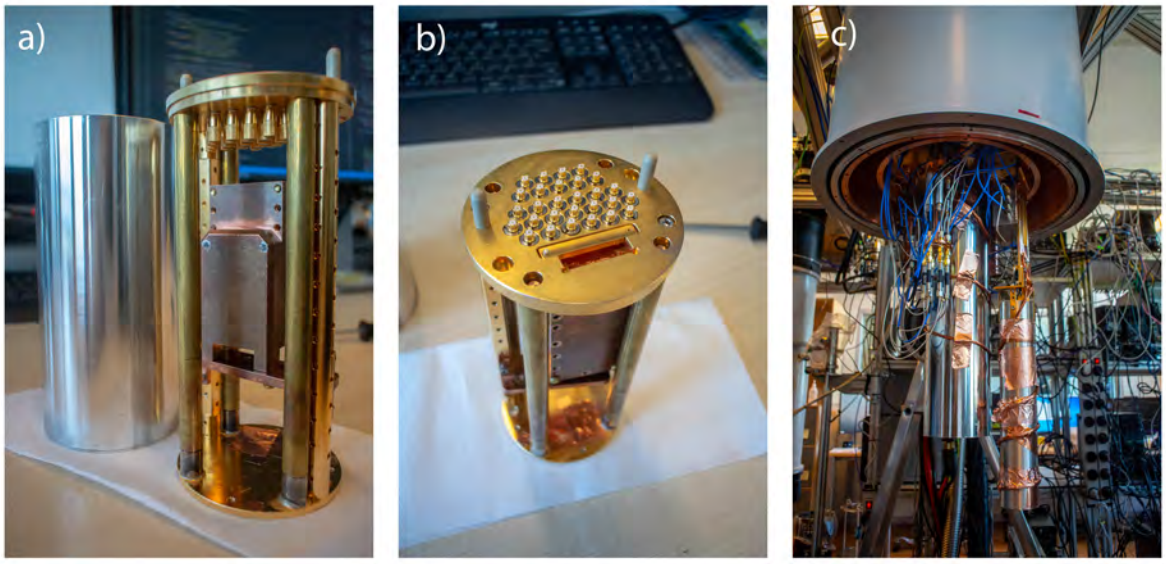

Figure 5.3: (a) Sample box mounted in puck (without any wires), (b) top connectors of the puck, and (c) dilution refrigerator in which he gatemon was loaded

5.2 Two-Tone Spectroscopy

After the gatemon was loaded, two-tone spectroscopy was done on it using the setup sketched in figure 5.4. We used a RF source to supply the constant resonator drive tone; freeing up the VNA to monitor this resonator tone while sweeping the qubit drive frequency. When the VNA hits the right qubit drive frequency, the qubit will be excited and thus exert a different push on the resonator frequency. The resonator drive tone will then experience an sudden shift in transmittance due to the changing resonator frequency; a shift which would then be quickly picked up by the VNA and correlated with the qubit drive frequency that caused it, effectively identifying the qubit energy.

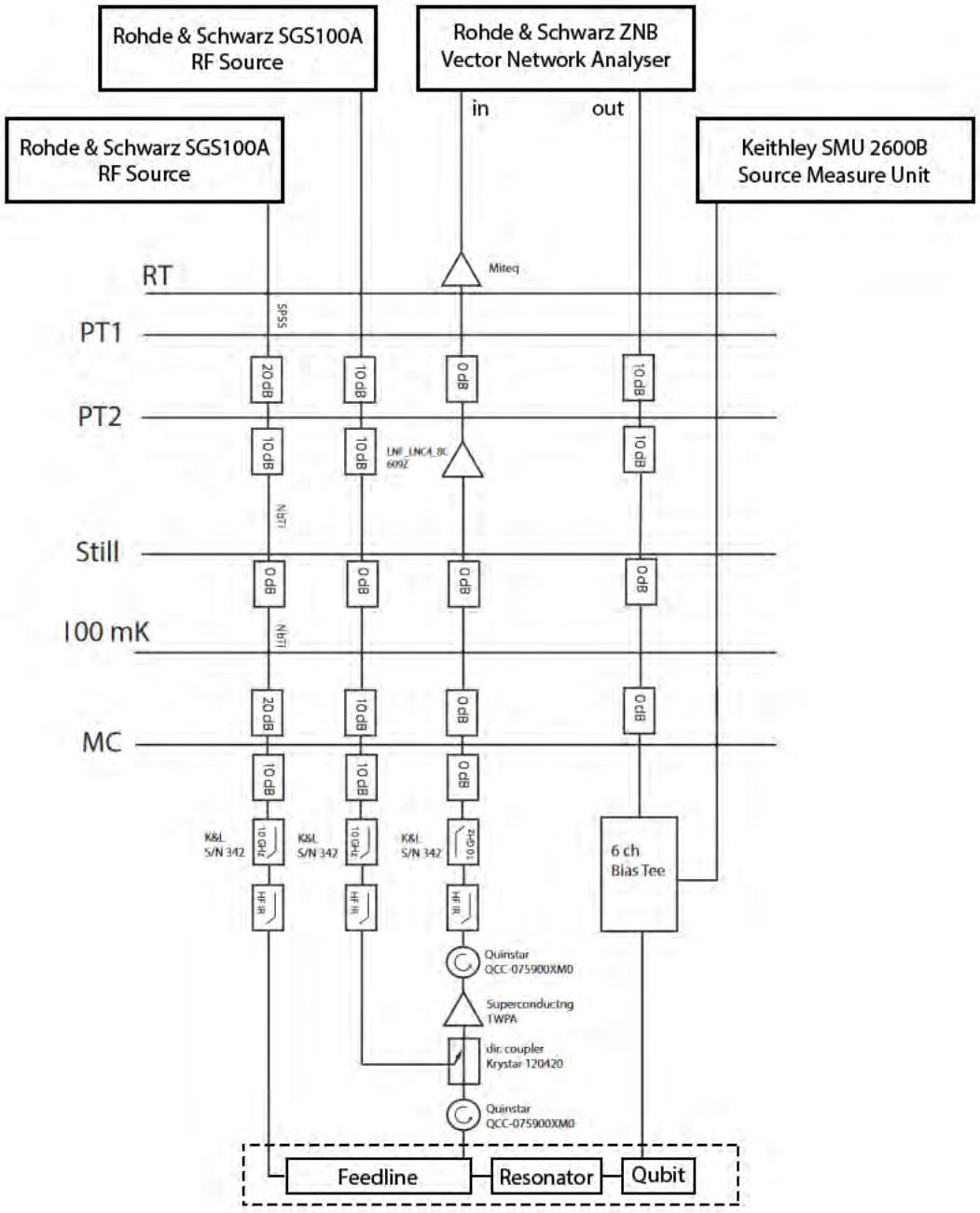

Figure 5.4: Two-tone spectroscopy setup around the fridge; where an RF source drives the resonator, and the VNA monitors this resonator drive while varying the qubit drive frequency.

This two-tone spectroscopy was first applied to track the gatemon frequency as the gate voltage was varied. The raw S_{21} transmittance measurements are plotted in figure 5.5a. The gatemon's spectroscopic signal can be seen here, but the background transmittance also varies quite a bit as the gate voltage is swept. Thus, we have also applied some background subtraction and smoothing across the different sweeps and across the gate voltages. This results in a much cleaner spectroscopic signal as plotted in figure 5.5b.

From these data, we can observe that the spectroscopic signal does generally move to lower frequencies as gate voltage decreases. This is as expected, since the 2DEG is moving closer to pinch-off and closer to essentially closed conduction channels. However, we also observe some non-monotonicity, with the qubit frequency tending to simply wobble back and forth across smaller voltage ranges. This is similar to what was seen in the previous 2DEG gatemon, although it is not known if there is underlying mechanism or if the many conduction channels are simply chaotically moving around [23].

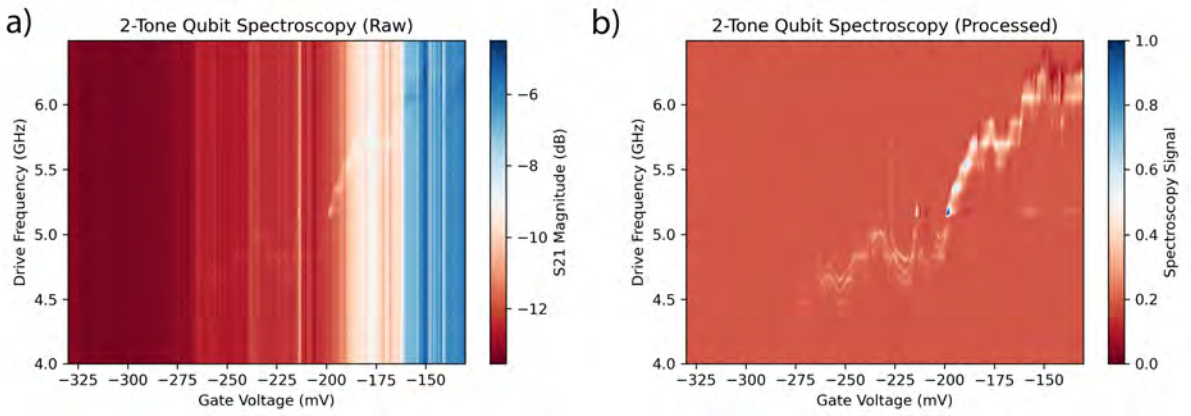

Figure 5.5: Two tone spectroscopy signals in terms of (a) raw S21 measurements, and (b) a background smoothened signal, as gate voltage is varied

We subsequently parked the gate voltage near the sweet spot at $-223\,\mathrm{mV}$ as identified in figure 5.5, before turning to track the spectroscopic signals' linewidth as qubit drive power is increased, as plotted in figure 5.6.

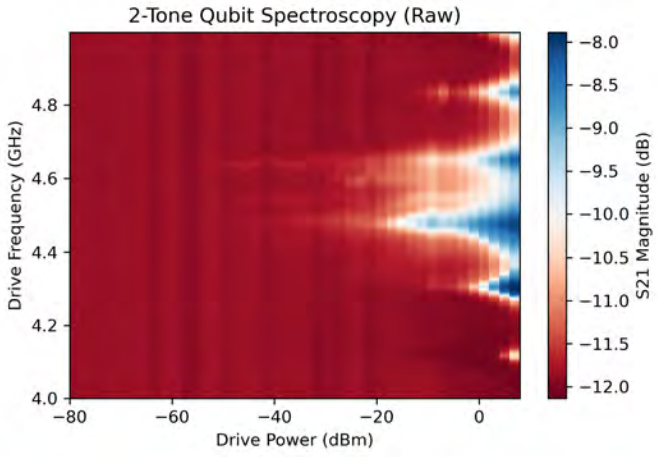

Figure 5.6: Two tone spectroscopy signal in terms of raw S21 measurement as qubit drive power is varied

It can be seen that the spectroscopic signal continue to exhibit qubit-like behaviour here. Firstly, as drive power increases to intermediate frequencies, additional spectroscopic signals start appearing. This is commonly seen with transmons, where they correspond to excitations to higher levels, possibly through multi-photon processes (i.e. $E_{02}/2, E_{12}$). It is also somewhat encouraging to see that the longest surviving state has the highest energy, suggesting that the qubit has negative anharmonicity as would be expected in the gatemon/tranmson regime.

As drive power increases even further, we observe that these spectroscopic signals exhibit power broadening. This is typically associated with anharmonic energy levels, since the power broadening results from a saturation of the excited state population in most cases. Additionally, we note that additional modes can also start appearing at these high drive powers such as at $-10\,\mathrm{dBm}$. However, these are likely just weakly-coupled stray environmental modes, which do not entail much.

Lastly, to more precisely estimate the anharmonicity of the qubit, we can measure the spectroscopic signal as the resonator readout power is lowered, as plotted in figure 5.7.

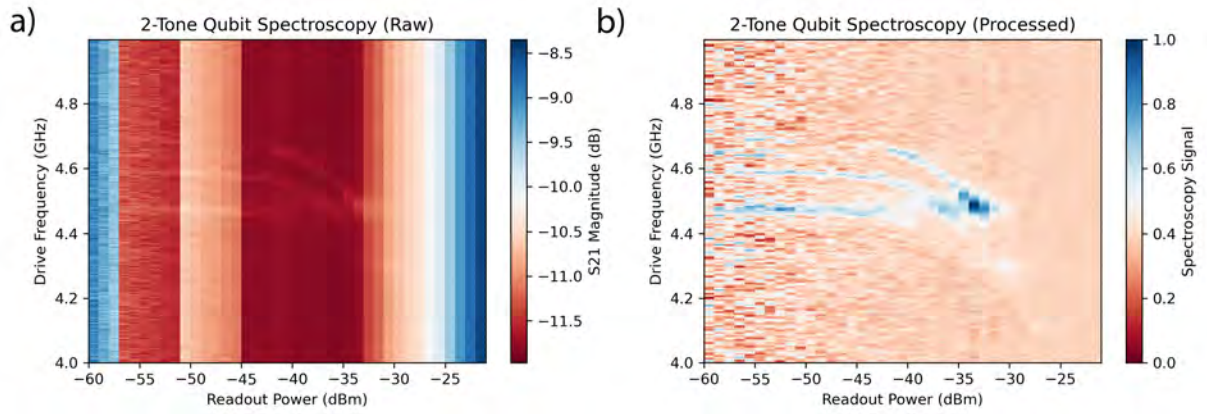

Figure 5.7: Two tone spectroscopy signals in terms of (a) raw S21 measurements, and (b) a background smoothened signal, as resonator readout power is varied

From this measurement, it is clear that the gatemon experiences significant AC Stark shift, as would be expected from the dispersive Jaynes-Cummings Hamiltonian. However, we are interested in the spectroscopic signal frequencies as the Stark shift becomes negligible. At these low powers, we observe that the three spectroscopic lines are roughly 100 MHz apart. If we then identify these to be E_{01}, $E_{02}/2 = E_{01} + \alpha/2$, $E_{12} = E_{01} + \alpha$, then we get an anharmonicity α of $-200\,\mathrm{MHz}$.

Comparing this anharmonicity to the expected charging energy of ∼230 MHz, we get following equation 3.9

$$1 - \frac{3\sum_i T_i^2}{4\sum T_i} \approx -\frac{\alpha}{E_C} \approx 0.9 \tag{5.1}$$

which suggests that the SNS junction in this gatemon has mostly lower transmission channels. However, we do not know what this entails for $\hat{n}$-parity qubit. As mentioned in section 3.4, these numerous lower transmission channels and their dominating 1st harmonic components might still destructively interfere and disappear in the $\hat{n}$-parity qubit.

6 2DEG $\hat{n}$-Parity Qubits

6.1 Current Progress

The move from the gatemon to the $\hat{n}$-parity qubit is conceptually simple: (1) make two identical junctions (2) from a loop with them (3) and add a flux-biasing line. This is exactly what we did, as can be seen in figure 6.1.

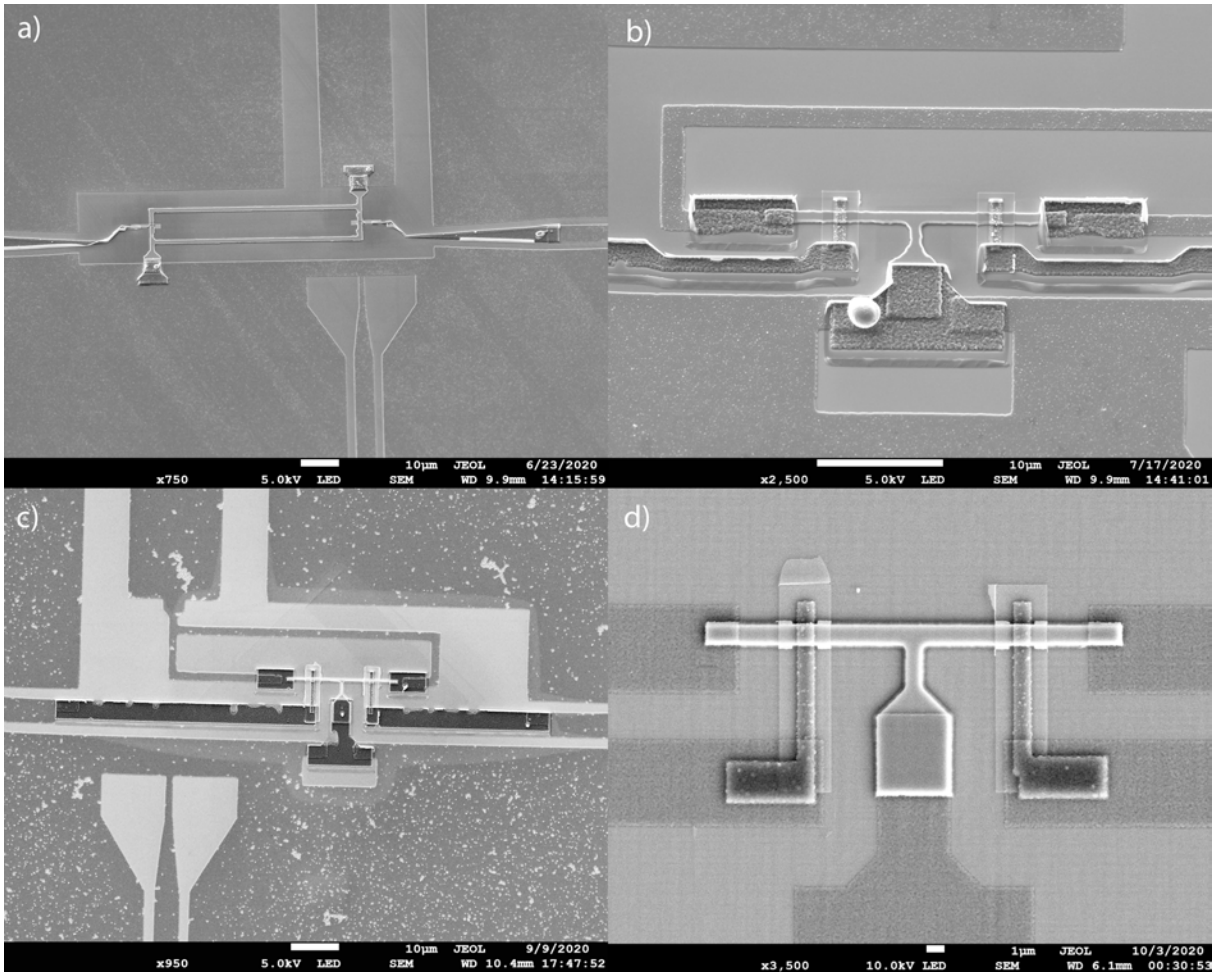

Figure 6.1: SEM micrographs of past, failed attempts at the $\hat{n}$-parity qubit

Unfortunately, none of the $\hat{n}$-parity qubits fabricated do far have given any cQED response; be it when flux-biasing, gate-biasing, or when pinching one of the junctions off to form a gatemon. We have iterated multiple times with improved design and fabrication process, but the devices have still not worked. This is what motivated us to take a step back and attempt a simpler 2DEG gatemon. Now that the gatemon seems to work, hopefully analysing it further will reveal what fixed it.

7 Conclusion

7.1 Summary

In this thesis, we first laid out the theoretical foundations for understanding qubits made from SNS junctions, and contrasted it with the conventional SIS ones. We then analysed the transmon, gatemon, and $\hat{n}$-parity qubit in a unified way using the integer $\hat{n}$ basis; allowing us to highlight how each qubit variant exactly differs from the other. With this knowledge in hand, we then proceeded to discuss the experimental aspect of realising these qubits. We described how a scalable 2DEG platform could be used to create SNS qubits, and used the methods in several attempts to create gatemons and $\hat{n}$-parity qubits. The gatemon was successful, and we did manage to see qubit-like spectroscopic signals whose behaviour gave some insights to our how our SNS junctions behave. The $\hat{n}$-parity qubits unfortunately have not seen much success yet. However, the recent success in the gatemon suggests that our material and fabrication methods are sound, and it might be useful to contrast the gatemon and $\hat{n}$-parity qubit design to see if there are any aspects that have been overlooked.

7.2 Outlook

The immediate problem that has to be overcome is clear: to continue figuring out how to make aspirant $\hat{n}$-parity qubits that at least gives some cQED response. Past that, it would be interesting to explore the overlooked offset-charge-sensitive regime of the $\hat{n}$-parity qubit, since the $\hat{n}$ protection would still be there, and the offset charge dispersion would make the states non-degenerate for simple cQED even in the protected regime. Additionally, it might also be worth questioning if the 3rd, 5th, and higher collective harmonics of the Andreev bound states could become significant, since having a single gate to balance the amplitudes of multiple higher harmonics could be a challenge.

Bibliography

[1] M. S. Rudolph, N. B. Toussaint, A. Katabarwa, S. Johri, B. Peropadre, and A. Perdomo-Ortiz, "Generation of high-resolution handwritten digits with an ion-trap quantum computer," *arXiv:2012.03924 [quant-ph]*, 2020. arXiv: 2012.03924.

[2] S. K. Kanungo *et al.*, "Realizing su-schrieffer-heeger topological edge states in rydberg-atom synthetic dimensions," *arXiv:2101.02871 [cond-mat, physics:physics]*, 2021. arXiv: 2101.02871.

[3] J. Koch *et al.*, "Charge-insensitive qubit design derived from the cooper pair box," *Physical Review A*, vol. 76, no. 4, p. 042 319, 2007, ISSN: 1050-2947, 1094-1622. DOI: 10.1103/PhysRevA.76.042319.

[4] N. A. Court, A. J. Ferguson, R. Lutchyn, and R. G. Clark, "Quantitative study of quasiparticle traps using the single-cooper-pair transistor," *Physical Review B*, vol. 77, no. 10, p. 100 501, 2008, ISSN: 1098-0121, 1550-235X. DOI: 10.1103/PhysRevB.77.100501.

[5] M. D. Reed *et al.*, "Fast reset and suppressing spontaneous emission of a superconducting qubit," *Applied Physics Letters*, vol. 96, no. 20, p. 203 110, 2010, ISSN: 0003-6951, 1077-3118. DOI: 10.1063/1.3435463.

[6] H. Paik *et al.*, "Observation of high coherence in josephson junction qubits measured in a three-dimensional circuit QED architecture," *Physical Review Letters*, vol. 107, no. 24, p. 240 501, 2011, ISSN: 0031-9007, 1079-7114. DOI: 10.1103/PhysRevLett.107.240501.

[7] L. B. Nguyen, Y.-H. Lin, A. Somoroff, R. Mencia, N. Grabon, and V. E. Manucharyan, "High-coherence fluxonium qubit," *Physical Review X*, vol. 9, no. 4, p. 041 041, 2019, Publisher: American Physical Society. DOI: 10.1103/PhysRevX.9.041041.

[8] A. Somoroff, Q. Ficheux, R. A. Mencia, H. Xiong, R. V. Kuzmin, and V. E. Manucharyan, "Millisecond coherence in a superconducting qubit," *arXiv:2103.08578 [cond-mat, physics:quant-ph]*, 2021. arXiv: 2103.08578.

[9] L. B. Ioffe and M. V. Feigel'man, "Possible realization of an ideal quantum computer in josephson junction array," *Physical Review B*, vol. 66, no. 22, p. 224 503, 2002, ISSN: 0163-1829, 1095-3795. DOI: 10.1103/PhysRevB.66.224503.

[10] S. Gladchenko, D. Olaya, E. Dupont-Ferrier, B. Douçot, L. B. Ioffe, and M. E. Gershenson, "Superconducting nanocircuits for topologically protected qubits," *Nature Physics*, vol. 5, no. 1, pp. 48–53, 2009, ISSN: 1745-2473, 1745-2481. DOI: 10.1038/nphys1151.

[11] M. T. Bell, J. Paramanandam, L. B. Ioffe, and M. E. Gershenson, "Protected josephson rhombus chains," *Physical Review Letters*, vol. 112, no. 16, p. 167 001, 2014, ISSN: 0031-9007, 1079-7114. DOI: 10.1103/PhysRevLett.112.167001.

[12] T. W. Larsen *et al.*, "Parity-protected superconductor-semiconductor qubit," *Physical Review Letters*, vol. 125, no. 5, p. 056 801, 2020, ISSN: 0031-9007, 1079-7114. DOI: 10.1103/PhysRevLett.125.056801.

[13] M. Tinkham, *Introduction to Superconductivity*, Second Edition, ser. International series in pure and applied physics. 36. New York: Mcgraw-Hill, 1995, 454 pp., ISBN: 0-07-064878-6.

[14] B. D. Josephson, "Coupled superconductors," *Reviews of Modern Physics*, vol. 36, no. 1, pp. 216–220, 1964. DOI: 10.1103/RevModPhys.36.216.

[15] R. P. Feynman, R. B. Leighton, and M. Sands, "The schrödinger equation in a classical context: A seminar on superconductivity," in *The Feynman Lectures on Physics*, The New Millenium Edition, vol. 3, New York: Basic Books, 2011, ISBN: 978-0-465-04083-4. [Online]. Available: https://www.feynmanlectures.caltech.edu/III_21.html.

[16] C. Rigetti *et al.*, "Superconducting qubit in a waveguide cavity with a coherence time approaching 0.1 ms," *Physical Review B*, vol. 86, no. 10, p. 100 506, 2012, ISSN: 1098-0121, 1550-235X. DOI: 10.1103/PhysRevB.86.100506.

[17] A. F. Andreev, "Thermal conductivity of the intermediate state of superconductors," *Soviet Journal of Experimental and Theoretical Physics*, vol. 19, no. 5, pp. 1228–1231, 1964. [Online]. Available: http://www.jetp.ac.ru/cgi-bin/dn/e_019_05_1228.pdf.

[18] C. W. J. Beenakker, "Universal limit of critical-current fluctuations in mesoscopic josephson junctions," *Physical Review Letters*, vol. 67, no. 27, pp. 3836–3839, 1991. DOI: 10.1103/PhysRevLett.67.3836.

[19] G. E. Blonder, M. Tinkham, and T. M. Klapwijk, "Transition from metallic to tunneling regimes in superconducting microconstrictions: Excess current, charge imbalance, and supercurrent conversion," *Physical Review B*, vol. 25, no. 7, pp. 4515–4532, 1982, ISSN: 0163-1829. DOI: 10.1103/PhysRevB.25.4515.

[20] T. Schäpers, *Superconductor/Semiconductor Junctions*, 1st Edition, ser. Springer Tracts in Modern Physics 174. Berlin: Springer-Verlag Berlin Heidelberg, 2001, ISBN: 978-3-540-45525-7. DOI: 10.1007/3-540-45525-6.

[21] Y. V. Nazarov and Y. M. Blanter, *Quantum Transport: Introduction to Nanoscience*. Cambridge: Cambridge University Press, 2009, ISBN: 978-0-521-83246-5. DOI: 10.1017/CBO9780511626906.

[22] D. J. van Woerkom *et al.*, "Microwave spectroscopy of spinful andreev bound states in ballistic semiconductor josephson junctions," *Nature Physics*, vol. 13, no. 9, pp. 876–881, 2017, ISSN: 1745-2481. DOI: 10.1038/nphys4150.

[23] L. Casparis *et al.*, "Superconducting gatemon qubit based on a proximitized two-dimensional electron gas," *Nature Nanotechnology*, vol. 13, no. 10, pp. 915–919, 2018, ISSN: 1748-3387, 1748-3395. DOI: 10.1038/s41565-018-0207-y.

Appendix: Detailed Fabrication Steps

Step	Description	Parameters
1.00	**Alignment Marks**	
1.01	Clean	Ace 5min, IPA 30s
1.02	Bake	185°C, 2min
1.03	Spin	A4, 4000rpm, 45s
1.04	Bake	185°C, 2min
1.05	Expose	680μC/cm2, 3nA, 125kV
		DXF: 1 Alignment layer, Heal
		PEC: 200nm PMMA on InP, 100% Contrast
1.06	Develop	MIBK:IPA 60s, IPA 10s
1.07	Ash	1 min
1.08	Evaporate	Ti, 10nm, 1Å/s, 0° tilt
1.09	Evaporate	Au, 50nm, 2Å/s, 0° tilt
1.10	Lift-off	Ace, RTP, 1h
1.11	Clean	IPA, 30s
2.00	**Mesa Etch**	
2.01	Bake	185°C, 2min
2.02	Spin	A4, 4000rpm, 45 s
2.03	Bake	185°C, 2min
2.04	Expose	500μC/cm2, 500pA, 100kV
		DXF: 2 Mesa Fine Biased 10um - 2 Mesa Fine, Inverted
		PEC: 200nm PMMA on InP, 100% Contrast
2.05	Expose	500μC/cm2, 40nA, 100kV, 300nm beam w/ 30nm pixel size
		DXF: 2 Mesa Fine Biased 10um + 2 Mesa Coarse, Inverted
		PEC: 200nm PMMA on InP, 0% Contrast
2.06	Develop	MIBK:IPA 30s, IPA 10s
2.07	Ash	1 min
2.08	Bake	115°C, 2min
2.09	Etch Al	Transene D 50°C 14s,
		MQ 50°C 20s, MQ RTP 40 s
2.10	Etch III-V	III-V etch 10min (MQ:C6H8O7:H3PO4:H2O2 = 220:55:3:3)
		MQ 30s, MQ 30s again
2.11	Strip	Dio 10min, Ace 5min, IPA 30s
3.00	**Control Layer**	
3.01	Bake	185°C, 2min
3.02	Spin	AR 300 80 NEW, 4000 rpm, 45s
3.03	Bake	185°C, 2min
3.04	Strip	Dio 2min, Ace 1min, IPA 30s
3.05	Bake	185°C, 2min
3.06	Spin	EL9, 4000rpm, 45s
3.07	Bake	185°C, 2min
3.08	Spin	CSAR13, 4000rpm, 45s
3.09	Bake	185°C, 2min
3.1	Expose	350μC/cm2, 100 nA, 125kV
		DXF: 3 Control Coarse, Control Medium, Control Fine
		PEC: 500nm CSAR on InP, 100% contrast
3.11	Develop	O-xy 30s, MIBK 1:3 30s, IPA 20s

3.12 Ash	1 min
3.13 Evaporate	Al, 100nm, 1Å/s, 0° tilt
3.14 Lift-off	Dio, RTP, Overnight
3.15 Ash	4 min
4.00 Junction Etch	
4.01 Bake	185°C, 2min
4.02 Spin	A4, 4000rpm, 45s
4.03 Bake	185°C, 2min
4.04 Expose	680µC/cm2, 500pA, 125kV DXF: 4 Junction Etch PEC: 200nm PMMA on InP, 100% Contrast
4.05 Develop	MIBK:IPA 30s, IPA 10s
4.06 Ash	1 min
4.07 Bake	115°C, 2min
4.08 Etch Al	Transene D 50˚C 13s, MQ 50˚C 20s, MQ RTP 40 s
4.09 Strip	Dio 10min, Ace 5min, IPA 30s
4.10 SEM	5 kV
4.10 Strip	Dio 5min, IPA 30s
5.00 Top Gate ALD	
5.01 Bake	185°C, 2min
5.02 Spin	A4, 4000rpm, 45s
5.03 Bake	185°C, 2min
5.04 Expose	680µC/cm2, 500pA, DXF: 5 Topgate ALD PEC: 200nm PMMA on InP, 100% Contrast
5.05 Develop	MIBK:IPA 30s, IPA 10s
5.06 Ash	1 min
5.07 ALD	HfO2, 150 cycles, 110°C, 10h pre-bake (total 25h)
5.09 Lift-off	Ace, 50°C, 2 hrs
6.00 Top Gate	
6.01 Bake	185°C, 2min
6.06 Spin	A4, 4000rpm, 45s
6.07 Bake	185°C, 2min
6.08 Expose	680µC/cm2, 100pA, DXF: 6 Topgate PEC: 200nm PMMA on InP, 100% Contrast
6.09 Develop	MIBK:IPA 60s, IPA 10s
6.10 Ash	1 min
6.11 Evaporate	Ti, 5nm, 1Å/s, 0° tilt
6.12 Evaporate	Al, 50nm, 1Å/s, 0° tilt
6.13 Lift-off	Ace, RTP, Overnight
6.14 Clean	IPA, 30s
7.00 Contacts	
7.01 Bake	185°C, 2min
7.02 Spin	EL9, 4000rpm, 45s
7.03 Bake	185°C, 2min

Appendix: Detailed Fabrication Steps

7.04	Spin	EL9, 4000rpm, 45s
7.05	Bake	185°C, 2min
7.06	Spin	A4, 4000rpm, 45s
7.07	Bake	185°C, 2min
7.08	Expose	680µC/cm2, 3nA, 500pA
		DXF: 7 Contacts
		PEC: 200nm PMMA on InP, 100% Contrast
7.09	Develop	MIBK:IPA 60s, IPA 10s
7.10	Ash	1 min
7.11	Kaufman mill	Ar, 15 sccm, 0.4mTorr, 0° tilt, Beam 300V
		Emission 46mA, Acceleration 120V, Discharge 40V
		Discharge 5 min, Warmup 2 min, Mill 4.5 min, Rest 2 min
7.12	Evaporate	Al, 350nm, 1Å/s, Rotation
		50nm @ 20°, 300nm @ 0°, 50nm @ 20°
7.13	Lift-off	Ace, RTP, overnight
7.14	Strip	Dio 10min, Ace 5min
7.14	Clean	IPA, 30s
8.00	**Bonding**	
8.01	Ash Chip	1min
8.02	Sonicate PCB	80kHZ, 100% power, 5min
8.03	Glue	A8, 2µL, Transmon Board
8.04	Bake	115°C, 3min
8.05	Bond	InPtoEpiAl program